THE JOURNAL OF PHYSICAL CHEMISTRY C

Article

pubs.acs.org/JPCC

Kinetics versus Charge Separation: Improving the Activity of Stoichiometric and Non-Stoichiometric Hematite Photoanodes Using a Molecular Iridium Water Oxidation Catalyst

Jonathon W. Moir,[†] Emma V. Sackville,[‡] Ulrich Hintermair,*[,‡] and Geoffrey A. Ozin*[,†]

[†]Department of Chemistry, University of Toronto, Toronto, Ontario M5S 3H6, Canada

[‡]Centre for Sustainable Chemical Technologies, University of Bath, Claverton Down, Bath BA2 7AY, U.K.

Supporting Information

ABSTRACT: Oxygen-deficient iron oxide thin films, which have recently been shown to be highly active for photoelectrochemical water oxidation, were surface-functionalized with a monolayer of a molecular iridium water oxidation cocatalyst. The iridium catalyst was found to dramatically improve the kinetics of the water oxidation reaction at both stoichiometric and nonstoichiometric α-Fe_2O_{3-x} surfaces. This was found to be the case in both the dark and in the light as evidenced by cyclic voltammetry, Tafel analysis, and electrochemical impedance spectroscopy (EIS). Oxygen evolution measurements under working conditions confirmed high Faradaic efficiencies of 69−100% and good stability over 22 h of operation for the functionalized electrodes. The resulting ∼200−300 mV shift in onset potential for the iridium-functionalized sample was attributed to improved interfacial charge transfer and oxygen evolution kinetics. Mott−Schottky plots revealed that there was no shift in flat-band potential or change in donor density following functionalization with the catalyst. The effect of the catalyst on thermodynamics and Fermi level pinning was also found to be negligible, as evidenced by open-circuit potential measurements. Finally, transient photocurrent measurements revealed that the tethered molecular catalyst did improve charge separation and increase charge density at the surface of the photoanodes, but only at high applied biases and only for the nonstoichiometric oxygen-deficient iron oxide films. These results demonstrate how molecular catalysts can be integrated with semiconductors to yield cooperative effects for photoelectrochemical water oxidation.

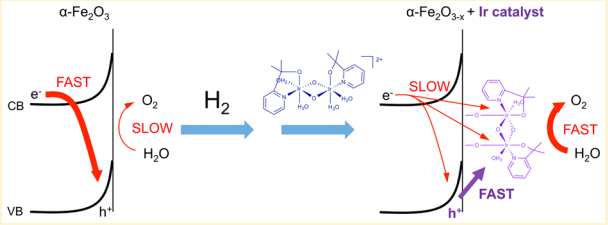

INTRODUCTION

The renewable production of clean, nonfossil-derived hydrogen is a critical part of a sustainable future economy, due to the importance of hydrogen in a variety of industrial applications including the Haber−Bosch process,[1] the Fischer−Tropsch process,[2,3] hydrogenation reactions, and organic transformations[4−6] and as transportation fuel in hydrogen fuel cells.[1,7] In principle, photoelectrochemical water splitting provides a facile route to clean hydrogen from water and enables simple monitoring of photoelectrode kinetics and activity.[8−14] Hematite (α-Fe_2O_3) is a primary photoanode candidate due to its many beneficial features including stability in aqueous alkaline media, Earth abundance, low toxicity, low cost, and its ability to theoretically absorb a large portion of the solar spectrum (∼18% of photons for AM1.5).[15] However, hematite's absorption coefficient is moderate at best (∼10^5 cm^{-1}, λ = 400−600 nm),[16−18] resulting in the need for nanostructured photoanodes in order to achieve high photocurrents.[19] In addition, defects and trap states as well as rapid recombination of photogenerated charge pairs have also limited hematite's photoactivity and resulted in high positive onset potentials for oxygen evolution from water.[20−23]

Recently it was shown that controlled thermal treatment of ultrathin films of hematite with hydrogen resulted in activation of the films toward the photoelectrochemical oxidation of water.[24] Using a variety of characterization techniques, it was determined that oxygen vacancies were present following the hydrogen treatment, resulting in a nonstoichiometric α-Fe_2O_{3-x} structure. The photoactivity was suggested to be a result of a change in Fermi level pinning or a decrease in electron−hole pair recombination following the H_2 treatment as a result of the n-type doping resulting from the presence of the intrinsic oxygen vacancies. A recent study by Forster et al. confirmed this latter effect for oxygen-deficient hematite photoanodes prepared in an oxygen-deficient atmosphere.[25] Transient absorption spectroscopy (TAS) and transient photocurrent (TPC) measurements performed *in situ* confirmed the buildup of photogenerated holes at the surface and a decrease in back electron−hole recombination due to a change in band bending close to the semiconductor−liquid junction (SCLJ). The results of these studies, along with other recent reports,[22,26,27] highlight the importance of charge separation in hematite photoanodes for efficient photoelectrochemical water oxidation.

Received: January 22, 2016
Revised: May 30, 2016
Published: June 1, 2016

DOI: 10.1021/acs.jpcc.6b00735
J. Phys. Chem. C 2016, 120, 12999−13012

While oxygen vacancies[28−30] and extrinsic dopants[31−34] are common methods of increasing charge carrier density and hence improving charge separation due to surface band bending,[35] cocatalysts,[36] and other surface modifiers[37] can also be used to improve photoactivity by increasing turnover, alleviating the effects of Fermi level pinning, or improving charge separation.[26,38−43] However, discerning unambiguously between one effect and another is not trivial,[16,44] and multiple effects may coexist or even be cooperative.

Most cocatalysts used in the oxygen evolution reaction (OER) are amorphous,[45−49] crystalline,[50−56] or pseudocrystalline[41,57−62] metal oxides or hydroxides. However, few examples exist to date of molecular cocatalysts in conjunction with heterogeneous photoanodes.[39,63−65] While there are many examples of homogeneous water oxidation catalysts (WOCs),[66−68] very few exhibit sufficient stability for sustained (photo)electrochemical water oxidation.[69−71] One exception to this is a recently reported iridium catalyst with the proposed structure $[Ir^{IV}(pyalk)(H_2O)_2(\mu\text{-}O)]_2^{2+}$ (see Scheme 1).[72,73]

Scheme 1. Oxidative Activation of the Cp*Ir(III) Precursor to the Electrochemically Active Ir(IV) Catalyst and Functionalization of the Dimer to the Iron Oxide Surface[a]

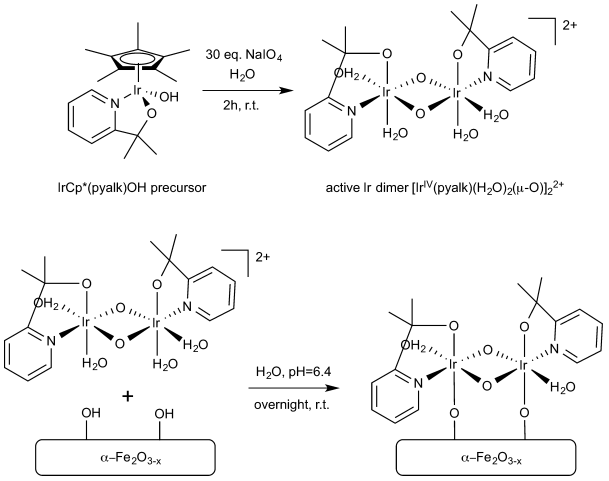

[a]Note that various coordination isomers of the activated iridium catalyst and numerous surface states on the α-Fe_2O_{3-x} will exist; thus, the diagram is purely illustrative.

The iridium(IV) oxy-dimer, formed by the chemical[74,75] or electrochemical[76] oxidation of an organometallic precursor such as [Cp*Ir(pyalk)OH], is extremely stable and highly active in oxygen evolution even under acidic conditions. In addition, it was most recently shown to bind strongly to metal oxide surfaces such as ITO in a spontaneous, self-limiting and irreversible process.[77] By virtue of a direct iridium−support bond, the so-obtained molecular monolayer is highly stable but itself not photoelectrochemically active.

Since this catalyst offers a unique opportunity to introduce a minimally thin layer of a stable water oxidation cocatalyst to the semiconductor-electrolyte interface, we wished to explore the interaction of this iridium WOC with our air-treated (photoelectrochemically inactive) α-Fe_2O_3 and our H_2-treated (photoelectrochemically active) oxygen-deficient α-Fe_2O_{3-x} thin films. A recent report[78] by Li et al. demonstrated the use of this molecular iridium catalyst and thin films of amorphous IrO_x for photoelectrochemical water oxidation using hydrothermally grown hematite photoanodes in acidic solution. However, more detailed electrochemical measurements, such as transient photocurrent measurements, were not undertaken at the time. [A more detailed study comparing the molecular iridium catalyst and IrO_x on hydrothermally grown hematite photoanodes appeared while this work was under review.[93]] In this work, testing of both our air-treated and H_2-treated films provided insight into the individual contributions of improved O_2 evolution kinetics, improved charge separation, and improved photovoltage when the iridium cocatalyst was present. This helped to elucidate the effect of the cocatalyst on photoanodes that exhibit decreased electron−hole pair recombination and increased charge separation under operating conditions (H_2-treated) as compared to those that do not (air-treated). Electrochemical impedance spectroscopy (EIS) and transient photocurrent (TPC) measurements were used to probe interfacial charge transfer resistances and charge recombination losses, respectively. Mott−Schottky analysis was used to evaluate changes to the flat-band potential of the photoanodes following hydrogen treatment and functionalization with the iridium catalyst. Finally, open circuit potential measurements were used to probe the effects of the catalyst on the overall photovoltage and Fermi level pinning.

EXPERIMENTAL METHODS

All reagents and solvents were used as received without further purification. Iron(III) nitrate nonahydrate (100.1% purity by ACS specifications) was purchased from J. T. Baker. Hydrogen peroxide solution (30 w/w%), ammonium hydroxide solution (28 v/v%), hydrochloric acid (37.5 w/w%), and sodium hydroxide pellets were purchased from Caledon. Fluorine-doped tin oxide (FTO) glass slides were purchased from Hartford Glass Inc.; these substrates were pretreated overnight in a 3:1 mixture of NH_4OH:H_2O_2, rinsed with 18.2 MΩ cm deionized (DI) water and stored in ethanol. Before the α-Fe_2O_3 precursor solution was spin-coated onto the FTO substrates, a small part of each glass electrode was covered by 3M transparent tape to allow for connection to the electrochemical equipment.

The precursor α-Fe_2O_3 solution was prepared according to previous reports.[24,79,80] Briefly, $Fe(NO_3)_3{\cdot}9H_2O$ (1.35 g) was added to a mixture of ethanol (12 mL) and DI water (3 mL) in a 20 mL scintillation vial and allowed to stir overnight at room temperature. Prior to spin-coating, the solution was filtered through a 0.45 μm syringe filter and diluted using a 4:1 solution of ethanol:water until the appropriate film thickness was acquired. Two 1″ × 1″ α-Fe_2O_3 films were created by spin-coating the filtered and diluted solution onto the FTO substrates using a Laurell Technologies spin-coater (model WS-400B-6NPP/LITE). Films were spun for 30 s at 3000 rpm at an acceleration of 4080 rpm/s. The samples were then annealed in air for 2 h using a Thermolyne 48000 muffle furnace. One sample was cut in half, with one-half being left bare (sample A) and the other half left to be functionalized with the iridium dimer (sample A−Ir, described below). The other large sample was treated in 5% H_2 (balance Ar, Praxair, flow rate of 15.9 sccm, maintained using a Matheson model 7632-600 flow meter) using a tube furnace (Thermo Scientific Lindberg/Blue M) at a ramp rate of 10 °C/min followed by thermal treatment at 600 °C for 2 h. This sample was then cut in half, with one-half being left bare (sample H) and the other half left to be functionalized with the iridium dimer (sample H−Ir, described below). The iridium precursor [IrCp*(pyalk)-OH] shown in Scheme 1 was synthesized according to previous

DOI: 10.1021/acs.jpcc.6b00735
J. Phys. Chem. C 2016, 120, 12999−13012

literature reports.[72] To generate the active iridium dimer, 14.5 mg (0.0302 mmol) of the precursor was added to 6.00 mL of DI water in an open 20 mL scintillation vial and the clear orange solution was stirred vigorously for 5 min. Under constant stirring, 30 equiv (205.4 mg, 0.960 mmol) of $NaIO_4$ was added to the vial and the dark blue solution was allowed to stir for 2 h at room temperature. The pH was then adjusted to between 6.4 and 7.2 using a solution of NaOH to avoid etching of the α-Fe_2O_3 thin films. Each of the films retained for functionalization (described above, samples A−Ir and H−Ir) was then immersed in the solution overnight, and the next day rinsed thoroughly with DI H_2O and stored in air on the benchtop. The reference FTO substrates used to measure the background tests were prepared by treating them in 3:1 NH_4OH:H_2O_2 solution overnight, in order to maximize surface coverage of OH groups and remove surface contaminants. Both substrates were washed thoroughly with DI water, and one of the substrates was then immersed in the iridium dimer solution overnight. The samples were immediately tested by cyclic voltammetry, chronopotentiometry and EIS (no heat treatment).

Hematite film thicknesses were estimated by measuring the UV−vis absorption spectra[27,81,82] of annealed films using a PerkinElmer Lambda 25 UV/vis spectrometer. Reflectance and transmittance were not taken into account; the thickness was estimated using a simple exponential absorption decay:

$$I = I_0 e^{-\alpha l} \tag{1}$$

where I is the transmitted intensity, I_0 is the incident beam intensity, l is the thickness in nm, and α is the absorption coefficient and is equal to 0.023 nm^{-1} at λ = 400 nm (a blank FTO slide was used for background correction).[17] Attenuated total reflectance Fourier-transform infrared (ATR-FTIR) spectra were acquired using a Thermo iS50 FTIR spectrometer. Raman spectra were acquired using a Bruker SENTERRA dispersive Raman microscope equipped with a 532 nm laser source and CCD detector (calibration is performed internally and automatically). Energy-dispersive X-ray (EDX) spectra were acquired using a QUANTA FEG 250 environmental scanning electron microscope (ESEM) equipped with an EDAX TEAM detector operating at 10 kV. X-ray photoelectron spectroscopy (XPS) was performed using a Thermo Scientific K-Alpha spectrometer. The spectra were acquired using an Al Kα X-ray source at a 90° incident angle to the sample with a 400 μm spot size. Deconvolution of the high resolution spectra was performed using Avantage software.

All electrochemical tests were performed in pH 7.3−7.4 solution (created by mixing solutions of 1.0 M HCl and 1.0 M NaOH) using a Ag/AgCl reference electrode and a Pt wire counter electrode. All potentials were adjusted to the reversible hydrogen electrode (RHE)[23,39,83] using the following equation:

$$E_{RHE} = E_{Ag/AgCl} + 0.197\ \text{V} + (0.059\ \text{pH}) \tag{2}$$

Here 0.197 V is the reference potential for Ag/AgCl at 25 °C.

All films were treated using chronopotentiometry for 1 h at ~50 $\mu A/cm^2$ in pH 7.3−7.4 electrolyte in order to stabilize the surface of the films and the tethered iridium catalyst. The films were then washed thoroughly with DI H_2O, and immersed in fresh electrolyte. Cyclic voltammetry (CV) was then performed from 0.42 to 1.62 V vs Ag/AgCl (~1.05 to 2.25 V vs RHE) using a Metrohm PGSTAT204 potentiostat at a scan rate of 20 mV/s. Five cycles were performed, with the first, third and fifth cycles performed in the dark, and the second and fourth cycles performed under 1 sun (100 mW/cm^2, calibrated using a Newport Oriel 91150V silicon reference cell) illumination using a 150 W Oriel Xe arc lamp (Newport 96000, 150W Xe ozone-free) equipped with an AM1.5G filter (Newport 81094). Tafel plots were derived from the final scan of the cyclic voltammetry measurements (performed in the dark). All CV and Tafel plots were adjusted to account for the series (or uncompensated) resistance through the system as measured using EIS. Chronoamperometry measurements were performed at 1.120 V vs Ag/AgCl (~1.75 V vs RHE); the samples were illuminated after 60 s using the same 1 sun illumination as for the CV measurements, and allowed to equilibrate for an additional 540 s. EIS measurements were performed using a Solartron SI 1260 impedance/gain-phase analyzer in conjunction with a Solartron SI 1287 instrument using Zplot software. Each sample was measured between 0.4 and 1.5 V vs Ag/AgCl (~1.03 and 2.13 V vs RHE) at 20 mV increments. Data were acquired between 100 000 and 0.1 Hz at a given potential, with a sinusoidal perturbation of ±10 mV. All of the Nyquist plots were modeled using Zview software with a Randles' equivalent circuit over the frequency range from ~0.1 to ~3000 Hz. Mott−Schottky plots were created by measuring the same samples using the same EIS conditions and equivalent circuit as above, but measuring between −0.230 and 0.490 V vs Ag/AgCl (~0.404 to 1.124 V vs RHE). The resulting capacitance C (Fcm^{-2}, samples referenced to their geometric surface area), derived from the constant phase element (CPE) of the equivalent circuit, was used to find the donor density N_d (cm^{-3}) and flat-band potential E_{fb} (V vs RHE) according to the following equation:[13,84]

$$\frac{1}{C^2} = \left[\frac{2}{q\varepsilon\varepsilon_0 N_d}\right]\left[E - E_{fb} - \left(\frac{kT}{q}\right)\right] \tag{3}$$

Here q is the charge on an electron, ε is the relative dielectric constant for hematite (32),[84,85] ε_0 is the permittivity of free space, E is the applied bias, k is Boltzmann's constant, and T is the temperature (298 K).

Transient photocurrent (TPC) measurements were performed using the Metrohm PGSTAT204 potentiostat and 150 W Oriel Xe arc lamp with AM1.5G filter described above. Samples were cycled three times in the dark from 0.42 to 1.62 V vs Ag/AgCl (~1.05 to 2.25 V vs RHE) immediately before starting the TPC measurements. All four samples were tested from 0.4 to 1.3 V vs Ag/AgCl (~1.03 to 1.93 V vs RHE) in 50 mV increments at a sampling rate of 200 points per second. Each sample was held at each potential for 30 s, with the broadband light source being turned on after 10 s and turned off after 20 s, before the next potential was applied. The exponential decay (following the light source being switched off after 20 s) was modeled using Origin 2015 (OriginLab) plotting and data analysis software. The biphasic exponential decay function used to model the current decay is as follows:

$$i = i_0 + Ae^{-t/\tau_1} + Be^{-t/\tau_2} \tag{4}$$

where i_0 is the plateau current at $t \gg 0$, A and B are constants, and τ_1 and τ_2 are the decay time constants of interest. τ_1 was found to be shorter than τ_2 in all cases. The cathodic charge passed was also analyzed using Origin 2015 software by integrating the area under each curve following the cathodic transient spike after ~20 s (labeled as "Q").

DOI: 10.1021/acs.jpcc.6b00735
J. Phys. Chem. C 2016, 120, 12999−13012

Oxygen evolution was measured using a custom-designed airtight photoelectrochemical cell placed inside of a N_2 glovebox (MBRAUN). Sample H−Ir was used as the working electrode along with a platinum wire counter electrode and a Ag/AgCl reference electrode. The film was tested in pH 7.4 solution which was thoroughly purged with N_2 before being brought into the glovebox. The sample was held at a potential of 1.12 V vs Ag/AgCl (or 1.75 V vs RHE) in the sealed cell, and was tested in the dark and under AM1.5G 1 sun illumination (100 mW/cm^2) for 24 and 22.4 h, respectively. Headspace measurements were performed at the beginning and at the end of each electrolysis run, and were analyzed using a gas chromatograph (Agilent 7820A) equipped with a TCD detector.

RESULTS AND DISCUSSION

The [Cp*Ir(pyalk)OH] precursor was synthesized according to previous reports.[72] The precursor was then activated by oxidation with 30 equiv of $NaIO_4$ in aqueous solution at room temperature for 2 h, as shown in Scheme 1 and as described in the Experimental Section.[77] Figure S1 (see Supporting Information) shows the UV−vis spectra of the iridium complex in solution before and after activation. The resulting dimer shows a characteristic blue color with a strong absorption feature at ∼620 nm, characteristic of the activated di-iridium(IV) bis-μ-oxo species.[74]

Hematite thin films were then synthesized for functionalization with the iridium dimer. Both air-treated α-Fe_2O_3 (photoelectrochemically inactive) and H_2-treated α-Fe_2O_{3-x} (photoelectrochemically active) thin films were prepared on FTO conductive glass substrates using a slightly modified version of our previous procedure.[24] Each film was then cut into two pieces: one piece of each film was functionalized with the iridium catalyst, according to the second part of Scheme 1, and the other piece was left bare. The result was four films for photoelectrochemical testing (see Scheme S1 in the Supporting Information): one air-treated α-Fe_2O_3 film (sample A), one air-treated α-Fe_2O_3 film functionalized with the iridium dimer (sample A−Ir), one H_2-treated α-Fe_2O_{3-x} film (sample H), and one H_2-treated α-Fe_2O_{3-x} film functionalized with the iridium dimer (sample H−Ir).

Films were characterized using UV−vis (Figure S2), attenuated total reflectance Fourier-transform infrared (ATR-FTIR, Figure S3), Raman (Figure S4), Energy Dispersive X-ray (EDX, Figure S5) and X-ray photoelectron (XPS, Figures S6 and S7) spectroscopic techniques. Film thicknesses were estimated from the UV−vis measurements to be ∼20 nm for samples A and A−Ir, and ∼25 nm for samples H and H−Ir (before H_2 treatment).[24] The ultrathin nature of the films was necessary as our previous results found that the photoactivity of the hydrogen-treated films decreased with increasing thickness beyond this regime,[24] likely due to the penetration depth of the hydrogen treatment. While we note that the photocurrents resulting from such ultrathin films are far from state-of-the-art, the samples provide an interesting case study for examining the difference between stoichiometric and nonstoichiometric photoanodes prepared from the same precursor.

Of the four spectroscopic measurements used, only XPS was sensitive enough to observe the molecular monolayer of iridium cocatalyst on the hematite surface (Figures S6 and S7). The deconvoluted high resolution spectra shown in Figure S7 show C−N, C−C, and C−O chemical environments, consistent with the presence of the pyalk ligand, as reported previously.[77,78] In addition, the ratio of N 1s:Ir $4f_{7/2}$:Ir $4f_{5/2}$ was found to be 2.2:1.0:1.0, consistent with a 1:1 ratio of N:Ir for the active $[Ir^{IV}(pyalk)(H_2O)_2(\mu\text{-}O)]_2^{2+}$ dimer.

Figure 1a shows the cyclic voltammetry results for the air-treated films. The films were tested at neutral pH (7.3−7.4)

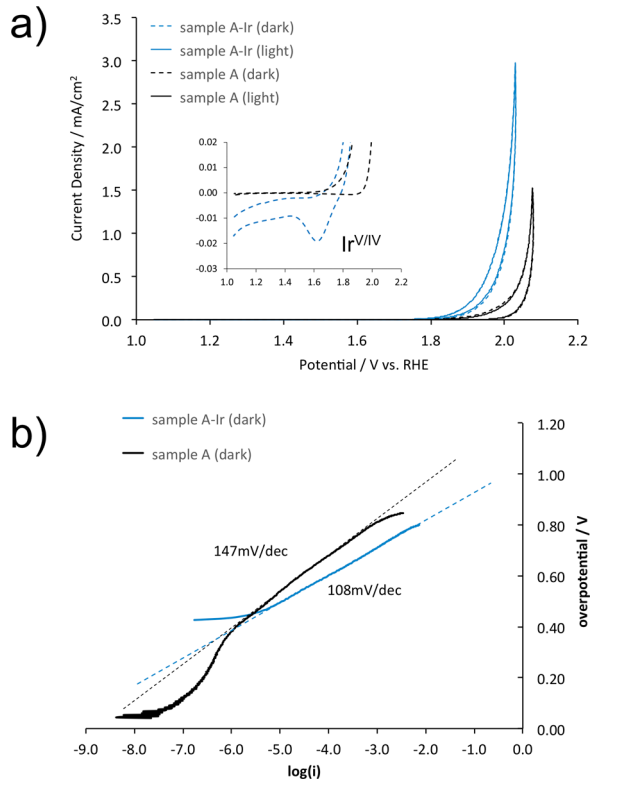

Figure 1. (a) Cyclic voltammograms of the air-treated α-Fe_2O_3 thin films before (sample A) and after (sample A−Ir) functionalization with the iridium cocatalyst. The light and dark cycles are the fourth and fifth scans, respectively, completed for each sample. The inset shows a close-up of the potential axis, where the reduction wave for the $Ir^{V/IV}$ couple can be seen on the reverse scan for sample A−Ir in the dark (the light scans are omitted in the inset for clarity). (b) Tafel plots derived from the cyclic voltammograms displayed in part a for samples A and A−Ir in the dark.

due to desorption of the iridium catalyst at high pH (∼13)[77] and dissolution of iron oxide at low pH. We reproducibly observed a substantial increase in dark current density for the iridium-functionalized samples at potentials >1.7 V vs RHE compared to the bare hematite films. Specifically, the overpotential for oxygen evolution at 0.5 mA/cm^2 was reduced from 870 to 760 mV (∼+2.10 to +1.99 V vs RHE), and from 950 to 830 mV (∼+2.18 to +2.06 V vs RHE) at 1.0 mA/cm^2. This is unlikely to be caused by a change in surface area, due to the reported stability of the iridium complex to particle formation,[72] the self-limiting nature of the surface functionalization, and the EIS results discussed further on. Instead, the iridium catalyst improves the kinetics of O_2 evolution at the surface in the dark as evidenced by the Tafel plots displayed in Figure 1b. The Tafel slopes are significantly reduced following iridium surface functionalization, yielding ∼147 mV/dec for sample A and 108 mV/dec for sample A−Ir, suggesting improved oxygen evolution kinetics for the iridium-functionalized films.

DOI: 10.1021/acs.jpcc.6b00735
J. Phys. Chem. C 2016, 120, 12999−13012

Following these promising data, we wished to explore the effect of the iridium cocatalyst on photocurrent and charge recombination in the air-treated films. While neither of the air-treated samples exhibited any large-scale photocurrent response (overlapping solid and dashed lines in Figure 1a), the peak current of the Ir^{V}/Ir^{IV} reduction wave[77,86] for sample A–Ir (inset of Figure 1a) was observed to decrease when the sample was illuminated during the reverse scan. On the next cycle, when the film was scanned in the dark again, the peak current would increase back to its original value. This reversible process was reproducible over multiple alternating dark and light cycles, as shown in Figure 2, parts a and b, indicating that photogenerated holes in the iron oxide film can be transferred to the iridium catalyst when under illumination, decreasing the number of electrochemically reducible iridium sites in the reverse scan (see Figure S8 for more details). This cooperative effect is confirmed by chronoamperometry measurements performed at 1.75 V vs RHE as shown in Figure 2c. The increase in current density exhibited by the iridium-functionalized films under biased illumination (inset of Figure 2c) shows that the cocatalyst facilitates the water oxidation reaction using photogenerated holes from the hematite film. However, the overall photocurrent is still extremely low, and is limited by recombination within the iron oxide film. Only a small fraction of the photogenerated holes are being transferred to the cocatalyst, likely due to the higher rate of recombination of electron–hole pairs in the hematite film close to the surface.[22,24,25] This is consistent with the TPC results described later on, which indicate there is no difference in the amount of charge available at the surface for the air-treated films before and after treatment with the cocatalyst. The rate of recombination within the hematite structure is therefore the limiting factor in these functionalized films.

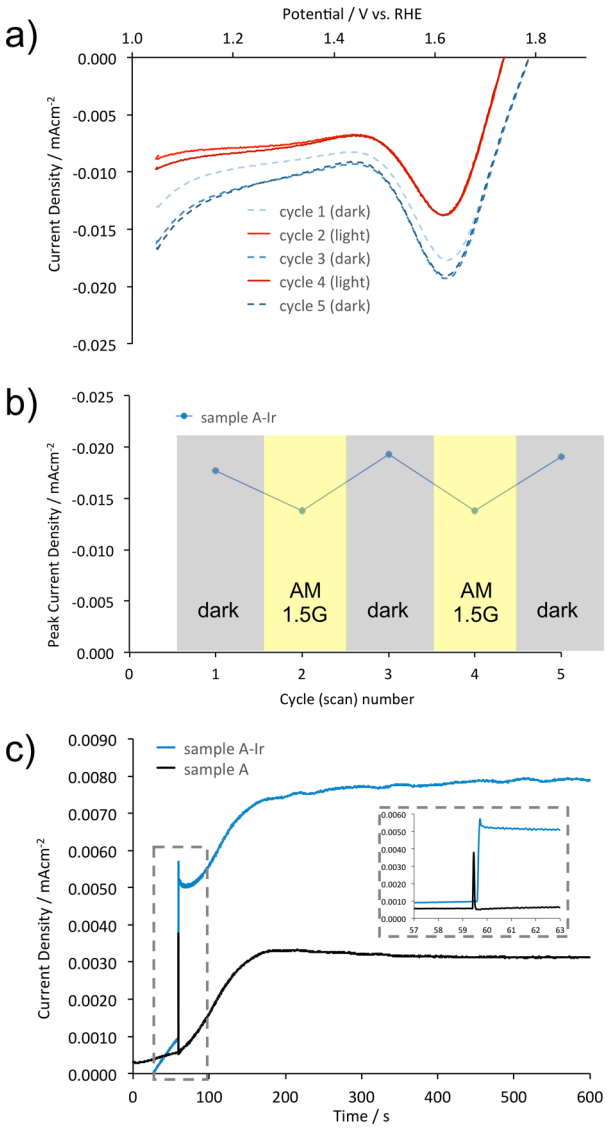

Figure 2. (a) Five cyclic voltammogram scans performed with sample A–Ir (the fourth and fifth scans are shown in Figure 1a, with the fifth scan shown in the inset). Only the reverse scans are shown for clarity. (b) Peak current at ~1.6 V as a function of cycle (scan) number derived from part a. (c) Chronoamperometry at 1.75 V vs RHE for samples A and A–Ir. Because 1.75 V vs RHE is close to the onset of dark electrolysis, background current is evident for both samples, plateauing after 200 s. The inset shows a zoom-in of the photocurrent response when the samples are illuminated after ~60 s.

Figure 3 shows the cyclic voltammetry results for the H_2-treated samples before (sample H) and after (sample H–Ir)

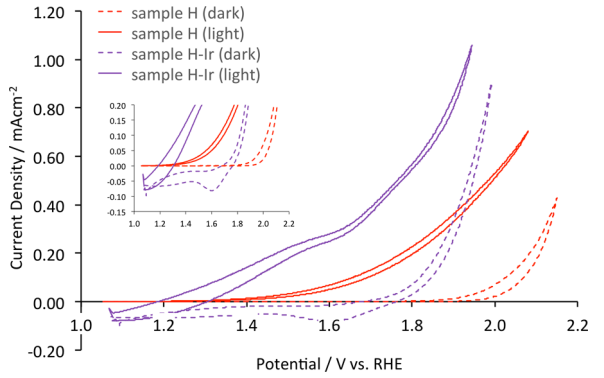

Figure 3. Cyclic voltammograms for the H_2-treated iron oxide film before (sample H) and after (sample H–Ir) functionalization with the Ir–WOC. The inset shows a zoom-in close to the potential axis where the $Ir^{V/IV}$ reduction wave is apparent in the dark for the film functionalized with the WOC.

functionalization with the iridium catalyst. In this case, both samples display strong and sustained photocurrents, due to a decrease in electron–hole pair recombination within the semiconductor following hydrogen treatment. However, the sample with the iridium catalyst shows a substantial increase in overall dark current (dashed line) despite identical geometric surface area. Specifically, the overpotential in the presence of the iridium catalyst is reduced from 914 to 684 mV (~+2.14 to +1.91 V vs RHE) at a current density of 0.4 mA/cm^2. This more substantial shift in overpotential when compared to the shift observed between samples A and A–Ir may stem from the increased loading of iridium catalyst on sample H–Ir compared to sample A–Ir. A comparison of peak currents (insets of Figures 1a and 3) shows about four times the peak current for the reduction wave of sample H–Ir compared to sample A–Ir. This increased loading may be a result of the hydrogen treatment, whereby a greater number of surface hydroxyl groups exist on the hematite surface following hydrogenation,[24,87] allowing for a greater loading of the iridium WOC as per Scheme 1. Sample H–Ir also shows a significantly greater photocurrent response than sample H (chronoamperometry

DOI: 10.1021/acs.jpcc.6b00735
J. Phys. Chem. C 2016, 120, 12999–13012

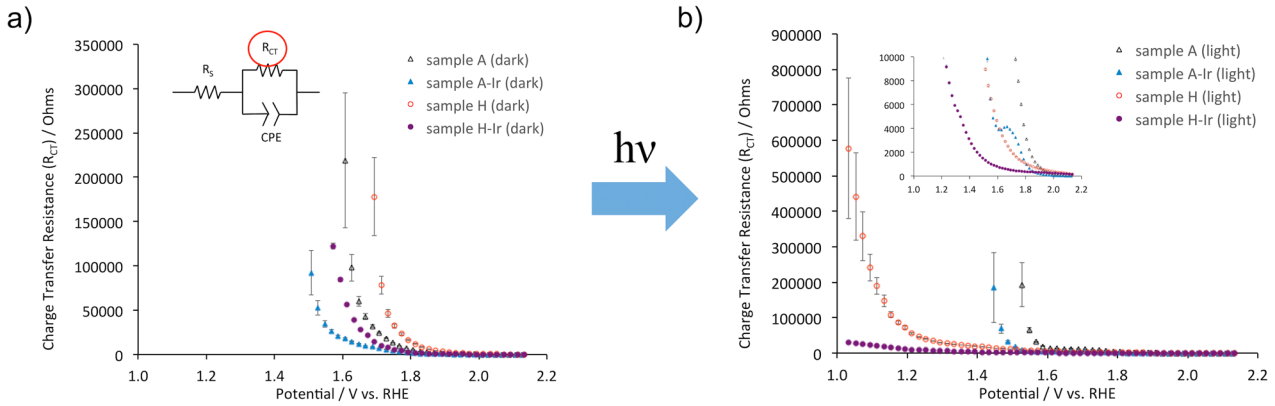

Figure 4. Charge transfer resistance (R_{CT}) vs potential for all four samples, modeled using a Randles' equivalent circuit. (a) Measured in the dark. The inset shows the circuit model and element in question. (b) Measured under AM1.5 1 sun illumination. The inset shows a zoom-in close to the potential axis.

results shown in Figure S9), with a shift in photocurrent onset potential of ∼200−300 mV across the entire potential window.

Oxygen evolution was confirmed for sample H−Ir using a custom-designed airtight photoelectrochemical reactor. The Faradaic efficiency was found to be 100% in the dark and 69% when under illumination (see Figures S10 and S11). This discrepancy may be due to slow corrosion of the copper tape used to connect the sample internally, or leaking of the cell due to increased internal pressure from formation of O_2 and H_2 when under illumination. The lower efficiency under illumination is unlikely to stem from reoxidation of the nonstoichiometric α-Fe_2O_{3-x} film, as full oxidation of a 25 nm film of α-Fe_2O_{3-x} (assuming x = 1 and accounting for a proportional decrease in density) at a current density of 0.2 mA/cm^2 would result in complete reoxidation of the film in 79 s. Regardless of the origin of this effect, even with this nonoptimized system we already observe significant formation of O_2 and H_2 and a strong cooperative photoeffect under long-term electrolytic conditions.

While the beneficial effect of the iridium catalyst on improving the activity of the films is obvious, we wished to verify the origin of the improved activity using more detailed experimental measurements. Specifically, we wished to explore in depth three possible routes by which the photoactivity could have been improved, namely: kinetic enhancement of interfacial charge transfer (oxygen evolution), decreased recombination losses at the semiconductor−liquid junction (charge separation), and improved photovoltage due to changes in Fermi level pinning.[16]

To begin, we used electrochemical impedance spectroscopy (EIS) to evaluate the various charge transfer processes and capacitive elements present at the semiconductor−liquid interface. Complex equivalent circuit models involving surface states that can store charge and/or mediate charge transfer have been used extensively to model hematite photoanodes under illumination.[23,84,88] These models are suitable when two semicircles are present in the Nyquist plots, each semicircle representing a different RC component with the smaller semicircle at higher frequencies generally representative of surface state trapping.[89] Previous work by Klahr et al. found that these models were suitable for hematite photoanodes prepared by atomic layer deposition (ALD) when under illumination at low applied biases; however when the samples were measured in the dark or at high applied biases only one semicircle was present, resulting in the use of a simple Randles' equivalent circuit.[84] While we observe a shoulder at high frequencies in the Nyquist plots for the samples treated with H_2 (Figure S12), this shoulder is present irrespective of the applied potential and regardless of whether the samples are illuminated or not. This may suggest that this feature is unrelated to a trapping process, and in fact more readily resembles anomalous transport behavior.[90,91] However, the exact reason for this behavior following hydrogen treatment is presently unclear and is beyond the scope of this study. Research into these effects is ongoing in our laboratory. Since the air-treated samples (Figure S12) and the FTO reference samples exhibited a single semicircle at all applied potentials (both in the dark and under illumination), all of the samples were therefore modeled using a Randles' equivalent circuit (shown in the inset of Figure 4a) at frequencies between ∼0.1 and ∼3000 Hz.

Parts a and b of Figure 4 show the R_{CT} values for all four samples in the dark and in the light, respectively, as a function of potential. For the samples functionalized with iridium, their charge transfer resistances are significantly lower at all measured potentials when compared to their nonfunctionalized counterparts. The H_2-treated films exhibited much lower R_{CT} values at low applied potentials when under illumination, as expected for films that can sustain photocurrents at these potentials. However, sample H−Ir showed substantially lower charge transfer resistances compared to sample H in this region. It therefore seems that the beneficial effect of the iridium catalyst is strongly kinetic in nature, which is consistent with the cyclic voltammetry results and the Tafel analysis. This is also consistent with another recent report that looked at R_{CT} for a ruthenium catalyst tethered to hematite nanorods grown on FTO,[39] and with a recent report looking at an electrodeposited IrO_x catalyst layer on silicon-doped α-Fe_2O_3 cauliflower-like photoanodes.[92]

While the charge transfer resistance was strongly affected by the presence of the cocatalyst, the capacitance did not change appreciably after functionalization with the iridium WOC. Figure S13 shows the capacitance derived from the constant phase element (CPE) as a function of potential for all four films. No appreciable difference was observed between the capacitances derived for the bare samples and the iridium-functionalized samples. This is not surprising given the monolayer coverage of the iridium catalyst, which would be unlikely to create a dielectric layer at the surface capable of appreciably modifying the bulk capacitance. However, it is possible that a redox capacitance could develop as a result of

DOI: 10.1021/acs.jpcc.6b00735
J. Phys. Chem. C 2016, 120, 12999−13012

the oxidized iridium centers around the point of the reduction wave observed in the inset of Figure 1a (~1.6 V vs RHE). To elucidate this further, and to avoid any capacitive contributions from the hematite layer, FTO substrates with and without the iridium catalyst were tested by EIS. The results, which are shown in Figure S14, parts a and b, reveal that there is a decrease in R_{CT} for the sample with iridium but again no significant change in capacitance, specifically around 1.6 V vs RHE. Furthermore, the cyclic voltammograms shown in Figure S14c indicate that the iridium is still present on the surface of the FTO after completion of the impedance measurements, ruling out degradation or desorption of the catalyst during the course of the measurements. These results are in excellent agreement with a recent report by Li et al. published while this study was under review.[93] The authors found using intensity modulated photocurrent spectroscopy (IMPS) and photoelectrochemical impedance spectroscopy (PEIS) that a surface-bound iridium cocatalyst improved the kinetics of the water oxidation reaction but did not alter the capacitance of the system. While the lack of a redox capacitance associated with the iridium centers may initially seem puzzling, Li et al. also suggested that the rate-limiting step for such a system was transfer of holes from the semiconductor to the cocatalyst, after which water oxidation is fast. If this is the case, no buildup of a redox peak would be expected under constant applied bias (such as during the EIS measurements). However, it is also possible that the capacitance is dominated by the space charge region in the semiconductor, and that the monolayer catalyst (similar to the Helmholtz double layer) does not contribute significantly to the total capacitance (in the case of capacitors in series) due to the short length scale over which this positive charge would be balanced by counteranions in solution. Nevertheless, we note that these results suggest that increases in activity due to surface area enhancement via IrO_x particle formation are unlikely, consistent with the reported stability of the iridium dimer.

The EIS data point toward a strong kinetic enhancement due to the tethered iridium catalyst, however the question remained as to whether improved charge separation could also play a role in enhancing the photoactivity of the films. To probe this, we used transient photocurrent (TPC) measurements and evaluated the decay of the photocurrent response (and the integrated charge passed) in the absence and presence of the iridium catalyst. Figure 5a shows a typical TPC chronoamperometry experiment for sample H−Ir upon turning on and off the broadband light source, along with the subsequent decay signal shown in the inset (Q represents the charge passed, or the area under the curve shaded in yellow). Previous reports have used monophasic exponential functions to model transient photocurrent decay signals for hematite photoanodes,[23,42,94] however, we found two linear regions in a logarithmic representation of our data (Figure S15) and obtained better R^2 fitting values using the biphasic function Equation 4 (see Table S1). Transient absorption spectroscopy (TAS) measurements on hematite photoanodes have generally been reported and modeled using biphasic exponential decays,[22,25,26] which have revealed two decay processes at the hematite-electrolyte interface: a bleach state ($\tau \approx 0.01-0.1$ s) associated with the filling of a trap state, and an increase in optical density due to long-lived valence band photoholes close to the surface ($\tau \approx 1$ s). Our results agree with the time scales of these measurements ($\tau_1 \approx 0.01-0.1$ s (Figure 5b) and $\tau_2 \approx 1-6$ s (Figure S16)). However, because TAS and TPC are very different

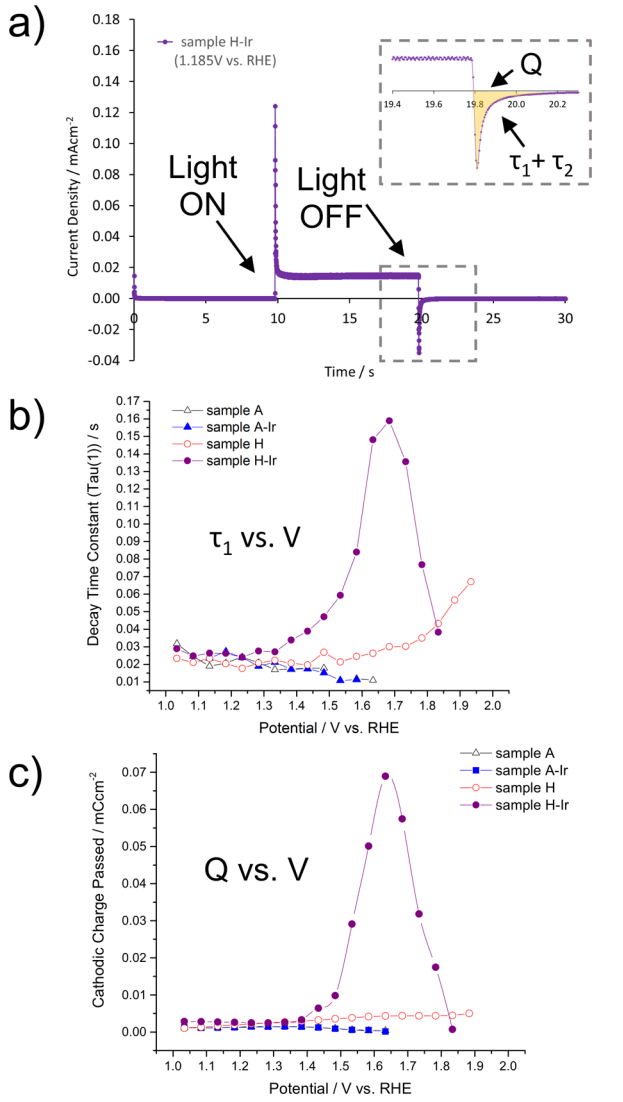

Figure 5. (a) Transient photocurrent (TPC) measurement for sample H−Ir. The decay of the photocurrent after 20 s following removal of the light source is shown in the inset, with the current decay profile represented by the two decay time constants (τ_1 and τ_2) and the total charge passed represented by the yellow shaded area (Q). (b) Decay constant τ_1 as a function of potential for all four samples (τ_2 vs V is shown in Figure S16). A zoom-in close to the potential axis is shown in Figure S17a. (c) Cathodic charge (Q) passed as a function of potential for all four films. A zoom-in close to the potential axis is shown in Figure S17b.

measurements, and TPC is a macroscopic technique, we cannot unambiguously identify the nature of these two decay processes at this time. As such, we attempt to make only a qualitative assessment of the difference in the decay response of the samples with and without the surface-bound iridium catalyst within this study.

Figure 5b shows the decay constant τ_1 as a function of potential for all four samples. Figure S17a shows a zoom-in close to the potential axis of Figure 5b, showing that there is essentially no difference between the decay response of samples A and A−Ir. It is well understood that the transient photocurrent response will be a convolution of the current associated with charge transfer of surface-bound holes (which will manifest as valence band holes, oxidized trap states, oxidized cocatalyst centers, or water oxidation intermediates) to

DOI: 10.1021/acs.jpcc.6b00735
J. Phys. Chem. C 2016, 120, 12999−13012

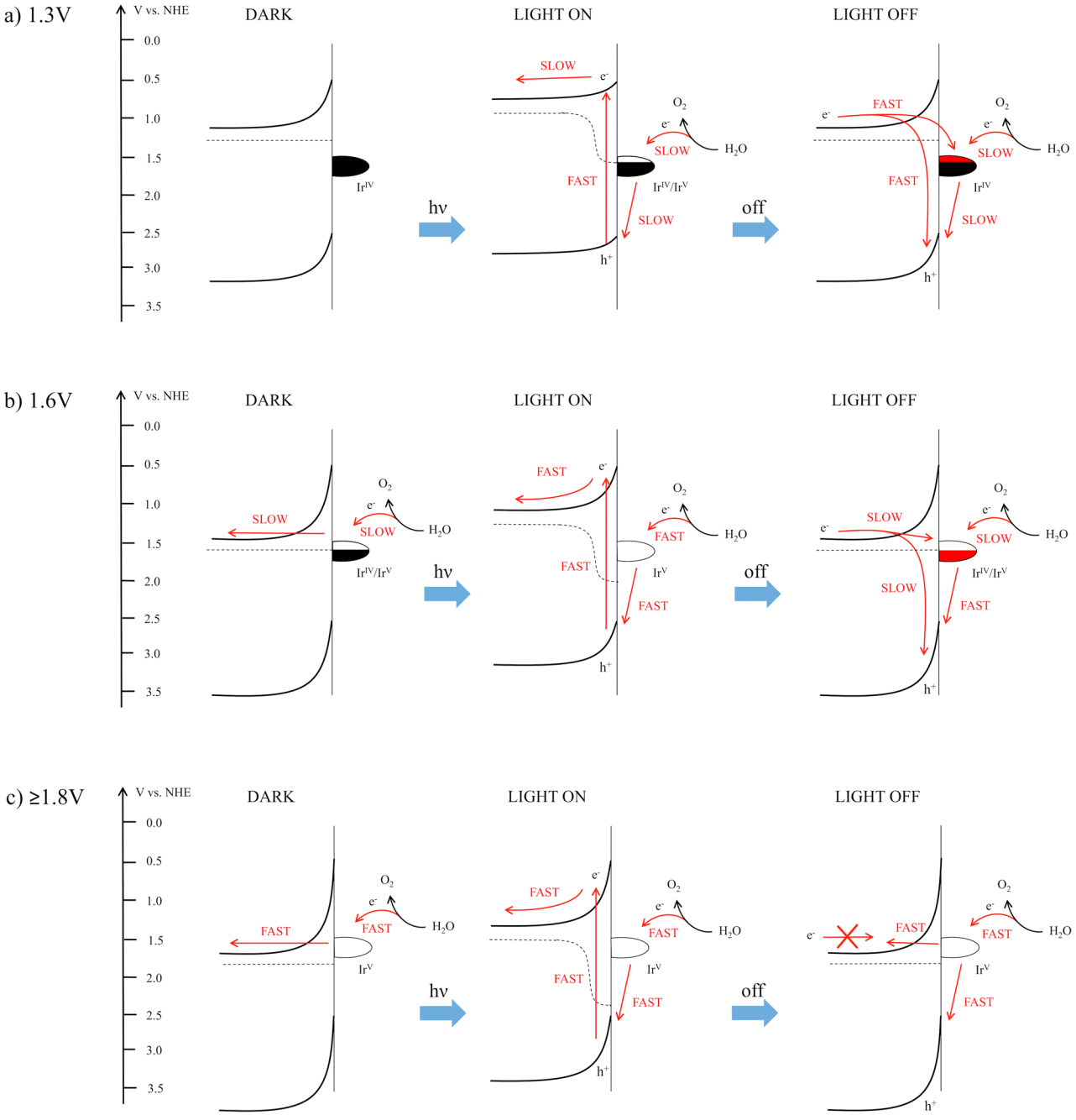

Figure 6. Band diagrams for sample H−Ir describing the flow of charge during a standard TPC experiment. The direction of electron flow is indicated in red. Solid black lines represent the conduction and valence bands of hematite, while the dotted lines represent the Fermi level within the semiconductor. The vertical lines represent the semiconductor-liquid interface, while the filled, partially filled and empty semicircles represent the degree of oxidation of the iridium catalyst molecules and the occupation of the Ir(IV) state. We note that surface states inherent to the hematite photoanode will likely also exist at the SCLJ, however we cannot undeniably confirm their existence or assign their energy levels at this time. As such, they have been omitted from the diagram. (a) At an applied potential of ∼1.3 V vs RHE. (b) At an applied potential of ∼1.6 V vs RHE. (c) At an applied potential of 1.8 V or higher vs RHE.

solution and the recombination of these surface-bound holes with majority carriers in the semiconductor (back electron recombination).[94,94−97] Since there is no steady-state photocurrent for the air-treated samples when the light is on, the rate of transfer of these surface-bound holes to solution must be close to zero (see Figure 2c). As a result, the transient current decay is solely a result of recombination of majority carriers with photoholes close to the surface. In this case, the presence of the iridium catalyst on the air-treated film does not change the rate of this electron−hole recombination (Figures 5b and S17a), nor does it change the density of photoholes at the surface (Figures 5c and S17b). The iridium catalyst therefore does not modify the charge recombination dynamics for air-treated hematite films that lack sufficient band bending to drive PEC water oxidation, and charge recombination out-competes charge transfer under illumination regardless of the presence of the cocatalyst or not. We again must note that the analysis is qualitative, and that the transient dynamics cannot unambiguously identify the nature of the recombination processes occurring at the surface of the films. Nevertheless, we can

DOI: 10.1021/acs.jpcc.6b00735
J. Phys. Chem. C 2016, 120, 12999−13012

establish thus far that the iridium WOC can provide a kinetic advantage for water oxidation in the dark for the air-treated samples (EIS and CV analysis), however it does not significantly alter the charge carrier dynamics of these air-treated films under illumination (TPC results).

Samples H and H−Ir display very different photocurrent decay responses than the air-treated films. Figure 5b shows a gradual increase in decay constant for sample H as a function of potential, which is correlated with a general increase in the cathodic charge passed (Figure 5c) and a general increase in photocurrent (Figure 3). Figure S17b shows that at a potential of +1.25 V vs RHE there is already twice the amount of charge passed (or twice the charge available at the surface) for sample H compared to sample A, and at +1.4 V vs RHE this value has risen to three times the amount of charge available. While the very presence of a cathodic transient suggests that there is still a large degree of recombination between majority carrier electrons and surface-bound photoholes (i.e., charge transfer to solution is slow, consistent with an incident photon-to-current efficiency (IPCE) of ∼2% reported previously),[24,97,98] the greater density of holes is not unexpected given the greater degree of band bending expected for an oxygen-deficient iron oxide photoanode.[25] This greater flux of holes to the surface is likely responsible for the photocurrent in the case of the hydrogen-treated films.[99] However, there is still room for improvement given the small difference in decay constants and cathodic transients between samples A, A−Ir, and H.

More interesting were the TPC results for sample H−Ir. An 8-fold increase in the decay constant for sample H−Ir was observed (Figure 5b) with a peak at ∼1.6 V (a similar trend was observed for τ_2, as shown in Figure S16). This was correlated with a 12-fold increase in the cathodic charge passed for sample H−Ir at the same peak position, as shown in Figure 5c. This suggests that the iridium catalyst, in the case of the hydrogen-treated films but not in the case of the air-treated films, can increase the density of surface-bound charge and decrease the rate at which majority carriers recombine with these surface-bound holes, specifically at the point where the Ir^{V}/Ir^{IV} reduction wave occurs.

The dynamics of this system can be illustrated using energy level diagrams, which are shown in Figure 6. At low applied potentials (∼1.3 V vs RHE, Figure 6a), there is no charge flow in the dark (i.e., water oxidation cannot occur). Upon illuminating the sample, a low water oxidation photocurrent is produced. A small number of holes build up at the surface, causing a hole quasi-Fermi level to induce some oxidation of the iridium catalyst and subsequently water oxidation. However, the number of oxidized iridium species is low due to the low concentration of holes, and the rate of water oxidation is also low as a result (high charge transfer resistance). The low rate of charge separation (high rate of recombination) means that, upon turning off the light, electrons rapidly flow back through the system to fill the holes at the surface. The low number of oxidized iridium centers means that there is little difference in the cathodic charge passed between samples H and H−Ir.

At moderate applied potentials (∼1.6 V vs RHE, Figure 6b), some of the iridium centers can now be oxidized up to the catalytically active state in the dark, and a small dark current can begin to flow, although the rate is still very low. Upon illumination, a larger number of the iridium centers are oxidized up into the catalytic regime due to the increase in band bending and surface-bound holes at these higher applied potentials. The greater concentration of holes results in a greater rate of water oxidation, and charge flow is considered "fast" at this point. Upon turning off the light, charge can now flow back to the surface from the bulk. However, because of the increased band bending, the flow of charge is slower, so the decay time constant is much higher. The reason the time constant is significantly greater for sample H−Ir compared to sample H is due to the tethered iridium catalyst. Charge is stored in the iridium centers (presumably as Ir(V)) and spatially separated to some extent from the majority charge carriers in the α-Fe_2O_{3-x}. This reduces the rate at which they recombine with the back-flow of electrons. In addition, at 1.6 V, the reduction wave for the iridium catalyst is observed in the cyclic voltammograms (Figures 1a and 3), meaning that at this potential the rate of reduction will be slowed based on simple electrochemical kinetics. The increase in cathodic charge passed is due to the buildup of charge stored in the iridium centers within the tethered catalyst molecules. Holes can now build up in significant numbers both in the iridium catalyst and in the hematite valence band. Upon turning off the illumination source, a greater number of electrons are required to fill these surface-bound holes, and a substantial increase in cathodic charge is observed. This charge buildup is not observed in the EIS results (Figure S13), however this lends support to the idea that the total capacitance of the system is dominated by the space charge region of the semiconductor, and that the iridium catalyst (similar to the Helmholtz double layer) has a negligible effect on the total capacitance of the system.

At even higher applied potentials (≥1.8 V vs RHE, Figure 6c), water oxidation readily occurs in the dark (we assume for simplicity that charge transfer occurs by tunneling through the surface to the conduction band of α-Fe_2O_{3-x}). Upon illumination, a photocurrent readily flows and all rates of electron transfer are "fast". When the light is turned off, the degree of band bending is too extreme for any back electron flow to occur, and the decay constant (and cathodic charge passed) rapidly falls off at higher and higher applied potentials to the point where back electron−hole recombination is no longer observed. However, the fact that this only occurs at very high applied potentials indicates that there is still room for improvement in terms of charge separation within the ultrathin hematite films. A truly efficient system should be able to separate charges at much lower applied potentials with much greater efficiency.

To evaluate the effect of band bending on these charge recombination processes, and to determine any change in the flat-band potential and donor density following hydrogen treatment and iridium functionalization, Mott−Schottky (MS) plots were created using capacitance values derived from the EIS measurements (Figure 7). From these data it is clear that following hydrogen treatment, the donor densities of samples H and H−Ir are significantly higher, by almost an order of magnitude, than their air-treated counterparts. Moreover, the flat-band potentials (E_{fb}) of the H_2-treated films are shifted to more negative potentials by almost 300 mV when compared to the E_{fb} values for samples A and A−Ir. The hydrogen treatment is therefore key to increasing the donor density within the film as a result of the creation of oxygen vacancies.[24,29,30] These vacancies create Fe^{2+} donor states that help to push the Fermi level of n-type α-Fe_2O_{3-x} toward the conduction band, resulting in a more negative flat-band potential and a greater degree of band bending at lower applied potentials.[25] This result is fully consistent with the TPC results above and the presence of a

DOI: 10.1021/acs.jpcc.6b00735
J. Phys. Chem. C 2016, 120, 12999−13012

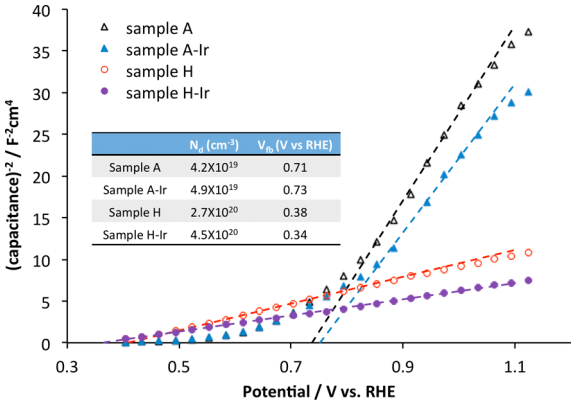

	N_d (cm^{-3})	V_{fb} (V vs RHE)
Sample A	4.2X10^{19}	0.71
Sample A-Ir	4.9X10^{19}	0.73
Sample H	2.7X10^{20}	0.38
Sample H-Ir	4.5X10^{20}	0.34

Figure 7. Mott–Schottky (MS) plots for all four samples. The dotted lines represent the linear extrapolation of the data to fit eq 3. The table in the inset shows the flat-band potentials (E_{fb}) and donor densities (N_d) derived from these linear regions.

photocurrent following hydrogen treatment. Importantly, however, the iridium cocatalyst on the surface does not appear to affect the flat-band potentials or donor densities of the hematite films, consistent with a recent report by Badia-Bou et al. on the effect of electrodeposited IrO_x on hematite photoanodes.[92]

Finally, to investigate whether the cocatalyst may also modify Fermi level pinning at the surface (a common issue for α-Fe_2O_3 photoanodes) by altering surface states and modifying band bending at the semiconductor-liquid junction,[12,13,16,38,42,100,101] we performed open-circuit potential (OCP) measurements, both in the dark and in the light, and measured the photovoltage of each film under AM1.5G 1 sun illumination.[48] Figure 8 shows the OCP values in the dark and in the light for

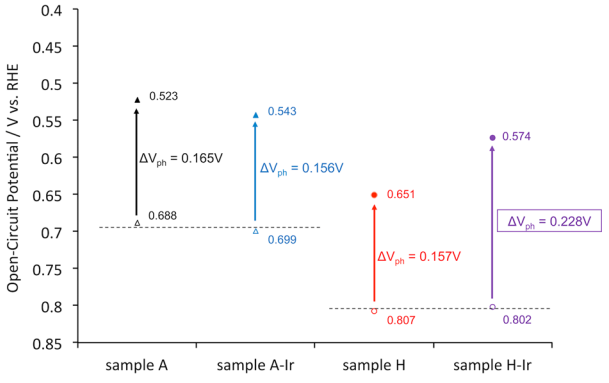

Figure 8. Open-circuit potential (OCP) measurements for all four samples. Measurements performed in the dark are shown with open symbols (more positive), while measurements performed under AM1.5G 1 sun illumination are shown with closed or solid symbols (more negative). The photovoltage measured for each sample is given as ΔV_{ph}. Dotted lines added to guide the eye.

all four samples performed in O_2 saturated solution. It should be noted that, since the potentials have been adjusted to the reversible hydrogen electrode (RHE), samples with no Fermi level pinning should exhibit an OCP in the dark close to +1.23 V.[38] Since none of the samples exhibit such a dark equilibrium potential, all four samples have some degree of Fermi level pinning. However, both air-treated samples have more negative dark OCP values than their hydrogen-treated counterparts. This indicates that the hydrogen treatment removes some of the Fermi level pinning and shifts the equilibrium potential toward the O_2/H_2O standard reduction potential. There is subsequently a greater degree of band bending at equilibrium (and at high applied potentials) for the H_2-treated samples. While there is still a photovoltage in the air-treated samples, their band bending must necessarily be insufficient under operating conditions (or the rate of recombination of electron–hole pairs must still be too high) for light-driven water oxidation to occur. These results are also consistent with the flat-band potentials measured in Figure 7: the air-treated films exhibit more positive flat-band potentials, which could be due to the presence of pinned states that prevent band bending from occurring until higher potentials are applied, while the hydrogen-treated films exhibit flat-band potentials closer to a "true" unpinned state. However, we note the difficulty in deconvoluting the effects of Fermi level pinning and increased donor density on the position of the flat-band potential from a Mott–Schottky analysis, as both effects would push the E_{fb} to more negative potentials.

Importantly, there is no effect on the photovoltage or equilibrium open-circuit potentials for the air-treated samples following functionalization with the iridium catalyst (sample A vs sample A–Ir). As such, the WOC does not alter Fermi level pinning at the surface of the hematite photoanode, and enhanced activity is a result of purely kinetic effects. This is consistent with the OCP results for the hydrogen-treated samples. Samples H and H–Ir also show similar OCP values in the dark, suggesting that the states on the hematite surface associated with Fermi level pinning are not affected by the iridium cocatalyst. However, one difference is observed in the photovoltage for sample H–Ir, which is higher than the photovoltage for the other three samples. This may again stem from the ability of the oxygen-deficient α-Fe_2O_{3-x} photoanode to transfer holes to the iridium centers, decreasing recombination under open-circuit conditions and increasing the quasi-Fermi level of holes, thus increasing the photovoltage. However, the 70 mV increase in photovoltage cannot completely account for the ~200–300 mV shift in photocurrent toward negative potentials, and kinetic factors are again the most important contribution toward the improved activity.

CONCLUSION

A stable molecular iridium water oxidation catalyst was successfully tethered to ultrathin hematite photoanodes, as confirmed using XPS and cyclic voltammetry. The iridium catalyst was found to improve the kinetic activity of both the air-treated α-Fe_2O_3 and H_2-treated α-Fe_2O_{3-x} films. In the case of the air-treated films, the iridium catalyst increased the electrocatalytic activity of the films in the dark, however transfer of photoholes from the hematite photoanode to the iridium catalyst was minimal due to insufficient band bending and high rates of recombination in the iron oxide, resulting in limited photoactivity. In the case of the H_2-treated films, the iridium catalyst not only improved the kinetics of the water oxidation reaction in both the dark and in the light, but also increased the density of photoholes at the surface and decreased the rate of recombination of majority charge carriers with these surface-bound charges at moderate to high applied potentials. This was confirmed by TPC measurements, whereby spatial separation of the hematite photoanode and the iridium cocatalyst resulted in an increase in the exponential decay time constants and a concomitant increase in positive charge present in the iridium centers, suggesting that both kinetic enhancements and

DOI: 10.1021/acs.jpcc.6b00735
J. Phys. Chem. C 2016, 120, 12999–13012

increased charge separation can readily occur for oxygen-deficient photoanodes that already exhibit sufficient band bending. Mott−Schottky plots revealed a shift in flat-band potential and increase in donor density following hydrogen treatment, however no change was observed when the iridium catalyst was present. OCP measurements also demonstrated that while there was a change in Fermi level pinning following hydrogen treatment, there was no change in Fermi level pinning following modification of the electrodes with the iridium cocatalyst monolayer. The effect of the catalyst was therefore almost entirely kinetic, and the studies presented herein will hopefully help to guide the future development of PV-catalyst tandem photoelectrochemical systems for improved light-driven water splitting.

■ ASSOCIATED CONTENT

Supporting Information

This material is available free of charge via the Internet at: The Supporting Information is available free of charge on the ACS Publications website at DOI: 10.1021/acs.jpcc.6b00735.

Film preparation, UV−vis, ATR-FTIR, Raman, EDX, and XPS spectra, plus additional electrochemical tests, EIS and TPC results, and O_2 and H_2 concentration measurements (PDF)

■ AUTHOR INFORMATION

Corresponding Authors

*(U.H.) E-mail: U.Hintermair@bath.ac.uk. Telephone: +44 (0) 1225 386682.

*(G.A.O.) E-mail: gozin@chem.utoronto.ca. Telephone: +1-416-487-9556.

Author Contributions

The manuscript was written through contributions of all authors. All authors have given approval to the final version of the manuscript.

Notes

The authors declare the following competing financial interest(s): US Patent Application Number 14/317,906 by U.H. et al. contains intellectual property described in this article. The other authors declare no competing financial interest.

■ ACKNOWLEDGMENTS

G.A.O. is the Government of Canada Research Chair in Materials Chemistry and Nanochemistry. We are deeply indebted to the Ontario Ministry of Research and Innovation (MRI) and the Ontario Ministry of Economic Development and Innovation (MEDI) for funding (Grant 492459). We are also grateful for strong and sustained support of our solar fuels research by the Natural Sciences and Engineering Research Council of Canada (NSERC, Grant 102723) and the Connaught Global Challenge Award (Grant 499222) through the University of Toronto. J.W.M. is grateful for an NSERC Canada Graduate Scholarship and for financial support from the Department of Chemistry at the University of Toronto. U.H. thanks the Centre for Sustainable Chemical Technologies at the University of Bath for a Whorrod Research Fellowship. E.V.S. acknowledges support from the EPSRC through the Centre for Doctoral Training in Sustainable Chemical Technologies (EP/L016354/1). The authors would like to thank Peter Brodersen (SI-Ontario) for help with XPS measurements and the machine shop in the Department of Chemistry at the University of Toronto for help with design and construction of the airtight photoelectrochemical cell.

■ ABBREVIATIONS

EIS, electrochemical impedance spectroscopy; TPC, transient photocurrent; MS, Mott−Schottky; ATR-FTIR, attenuated total reflectance Fourier-transform infrared; CV, cyclic voltammetry; XPS, X-ray photoelectron spectroscopy; EDX, energy-dispersive X-ray; OCP, open-circuit potential; WOC, water oxidation catalyst

■ REFERENCES

(1) Armaroli, N.; Balzani, V. The Hydrogen Issue. *ChemSusChem* **2011**, *4*, 21−36.

(2) Khodakov, A. Y.; Chu, W.; Fongarland, P. Advances in the Development of Novel Cobalt Fischer−Tropsch Catalysts for Synthesis of Long-Chain Hydrocarbons and Clean Fuels. *Chem. Rev.* **2007**, *107*, 1692−1744.

(3) Schulz, H. Short History and Present Trends of Fischer−Tropsch Synthesis. *Appl. Catal., A* **1999**, *186*, 3−12.

(4) Behr, A.; Vorholt, A. J.; Seidensticker, T. An Old Friend in a New Guise-Recent Trends in Homogeneous Transition Metal Catalysis. *ChemBioEng Rev.* **2015**, *2*, 6−21.

(5) O'Brien, P. G.; Sandhel, A.; Wood, T. E.; Jelle, A. A.; Hoch, L. B.; Perovic, D. D.; Mims, C. A.; Ozin, G. A. Photomethanation of Gaseous CO_2 over Ru/Silicon Nanowire Catalysts with Visible and Near-Infrared Photons. *Adv. Sci.* **2014**, *1*, 1400001.

(6) Hoch, L. B.; Wood, T. E.; O'Brien, P. G.; Liao, K.; Reyes, L. M.; Mims, C. A.; Ozin, G. A. The Rational Design of a Single-Component Photocatalyst for Gas-Phase CO_2 Reduction Using Both UV and Visible Light. *Adv. Sci.* **2014**, *1*, 1400013.

(7) Yilanci, A.; Dincer, I.; Ozturk, H. K. A Review on Solar-Hydrogen/Fuel Cell Hybrid Energy Systems for Stationary Applications. *Prog. Energy Combust. Sci.* **2009**, *35*, 231−244.

(8) Osterloh, F. E. Inorganic Nanostructures for Photoelectrochemical and Photocatalytic Water Splitting. *Chem. Soc. Rev.* **2013**, *42*, 2294−2320.

(9) Grätzel, M. Photoelectrochemical Cells. *Nature* **2001**, *414*, 338−344.

(10) Walter, M. G.; Warren, E. L.; McKone, J. R.; Boettcher, S. W.; Mi, Q.; Santori, E. A.; Lewis, N. S. Solar Water Splitting Cells. *Chem. Rev.* **2010**, *110*, 6446−6473.

(11) Lewis, N. S.; Nocera, D. G. Powering the Planet: Chemical Challenges in Solar Energy Utilization. *Proc. Natl. Acad. Sci. U. S. A.* **2006**, *103*, 15729−15735.

(12) Yang, X.; Liu, R.; He, Y.; Thorne, J.; Zheng, Z.; Wang, D. Enabling Practical Electrocatalyst-Assisted Photoelectrochemical Water Splitting with Earth Abundant Materials. *Nano Res.* **2015**, *8*, 56−81.

(13) Smith, W. A.; Sharp, I. D.; Strandwitz, N. C.; Bisquert, J. Interfacial Band-Edge Energetics for Solar Fuels Production. *Energy Environ. Sci.* **2015**, *8*, 2851−2862.

(14) Ager, J. W.; Shaner, M. R.; Walczak, K. A.; Sharp, I. D.; Ardo, S. Experimental Demonstrations of Spontaneous, Solar-Driven Photoelectrochemical Water Splitting. *Energy Environ. Sci.* **2015**, *8*, 2811−2824.

(15) Sun, J.; Zhong, D. K.; Gamelin, D. R. Composite Photoanodes for Photoelectrochemical Solar Water Splitting. *Energy Environ. Sci.* **2010**, *3*, 1252−1261.

(16) Iandolo, B.; Wickman, B.; Zorić, I.; Hellman, A. The Rise of Hematite: Origin and Strategies to Reduce the High Onset Potential for the Oxygen Evolution Reaction. *J. Mater. Chem. A* **2015**, *3*, 16896−16912.

(17) Marusak, L. A.; Messier, R.; White, W. B. Optical Absorption Spectrum of Hematite, α-Fe_2O_3 near IR to UV. *J. Phys. Chem. Solids* **1980**, *41*, 981−984.

DOI: 10.1021/acs.jpcc.6b00735
J. Phys. Chem. C 2016, 120, 12999−13012

(18) Sivula, K. Nanostructured α-Fe_2O_3 Photoanodes. In *Photoelectrochemical Hydrogen Production*; van de Krol, R., Grätzel, M., Eds.; Springer Science and Business Media: New York, 2012; pp 121−156.
(19) Wheeler, D. A.; Wang, G.; Ling, Y.; Li, Y.; Zhang, J. Z. Nanostructured Hematite: Synthesis, Characterization, Charge Carrier Dynamics, and Photoelectrochemical Properties. *Energy Environ. Sci.* **2012**, *5*, 6682−6702.
(20) Sivula, K. Metal Oxide Photoelectrodes for Solar Fuel Production, Surface Traps, and Catalysis. *J. Phys. Chem. Lett.* **2013**, *4*, 1624−1633.
(21) Sivula, K.; Le Formal, F.; Grätzel, M. Solar Water Splitting: Progress Using Hematite (α-Fe_2O_3) Photoelectrodes. *ChemSusChem* **2011**, *4*, 432−449.
(22) Barroso, M.; Pendlebury, S. R.; Cowan, A. J.; Durrant, J. R. Charge Carrier Trapping, Recombination and Transfer in Hematite (α-Fe_2O_3) Water Splitting Photoanodes. *Chem. Sci.* **2013**, *4*, 2724−2734.
(23) Le Formal, F.; Pendlebury, S. R.; Cornuz, M.; Tilley, S. D.; Grätzel, M.; Durrant, J. R. Back Electron−Hole Recombination in Hematite Photoanodes for Water Splitting. *J. Am. Chem. Soc.* **2014**, *136*, 2564−2574.
(24) Moir, J.; Soheilnia, N.; Liao, K.; O'Brien, P.; Tian, Y.; Burch, K. S.; Ozin, G. A. Activation of Ultrathin Films of Hematite for Photoelectrochemical Water Splitting via H_2 Treatment. *ChemSusChem* **2015**, *8*, 1557−1567.
(25) Forster, M.; Potter, R. J.; Ling, Y.; Yang, Y.; Klug, D. R.; Li, Y.; Cowan, A. J. Oxygen Deficient α-Fe_2O_3 Photoelectrodes: A Balance between Enhanced Electrical Properties and Trap-Mediated Losses. *Chem. Sci.* **2015**, *6*, 4009−4016.
(26) Barroso, M.; Mesa, C. A.; Pendlebury, S. R.; Cowan, A. J.; Hisatomi, T.; Sivula, K.; Grätzel, M.; Klug, D. R.; Durrant, J. R. Dynamics of Photogenerated Holes in Surface Modified α-Fe_2O_3 Photoanodes for Solar Water Splitting. *Proc. Natl. Acad. Sci. U. S. A.* **2012**, *109*, 15640−15645.
(27) Hisatomi, T.; Dotan, H.; Stefik, M.; Sivula, K.; Rothschild, A.; Grätzel, M.; Mathews, N. Enhancement in the Performance of Ultrathin Hematite Photoanode for Water Splitting by an Oxide Underlayer. *Adv. Mater.* **2012**, *24*, 2699−2702.
(28) Wang, G.; Ling, Y.; Li, Y. Oxygen-Deficient Metal Oxide Nanostructures for Photoelectrochemical Water Oxidation and Other Applications. *Nanoscale* **2012**, *4*, 6682−6691.
(29) Ling, Y.; Wang, G.; Wang, H.; Yang, Y.; Li, Y. Low-Temperature Activation of Hematite Nanowires for Photoelectrochemical Water Oxidation. *ChemSusChem* **2014**, *7*, 848−853.
(30) Yang, T.-Y.; Kang, H.-Y.; Sim, U.; Lee, Y.-J.; Lee, J.-H.; Koo, B.; Nam, K. T.; Joo, Y.-C. A New Hematite Photoanode Doping Strategy for Solar Water Splitting: Oxygen Vacancy Generation. *Phys. Chem. Chem. Phys.* **2013**, *15*, 2117−2124.
(31) Kleiman-Shwarsctein, A.; Hu, Y.-S.; Forman, A. J.; Stucky, G. D.; McFarland, E. W. Electrodeposition of α-Fe_2O_3 Doped with Mo or Cr as Photoanodes for Photocatalytic Water Splitting. *J. Phys. Chem. C* **2008**, *112*, 15900−15907.
(32) Ling, Y.; Li, Y. Review of Sn-Doped Hematite Nanostructures for Photoelectrochemical Water Splitting. *Part. Part. Syst. Charact.* **2014**, *31*, 1113−1121.
(33) Zhang, M.; Luo, W.; Li, Z.; Yu, T.; Zou, Z. Improved Photoelectrochemical Responses of Si and Ti Codoped α-Fe_2O_3 Photoanode Films. *Appl. Phys. Lett.* **2010**, *97*, 042105.
(34) Steier, L.; Herraiz-Cardona, I.; Gimenez, S.; Fabregat-Santiago, F.; Bisquert, J.; Tilley, S. D.; Grätzel, M. Understanding the Role of Underlayers and Overlayers in Thin Film Hematite Photoanodes. *Adv. Funct. Mater.* **2014**, *24*, 7681−7688.
(35) Katz, M. J.; Riha, S. C.; Jeong, N. C.; Martinson, A. B. F.; Farha, O. K.; Hupp, J. T. Toward Solar Fuels: Water Splitting with Sunlight and "rust"? *Coord. Chem. Rev.* **2012**, *256*, 2521−2529.
(36) Li, X.; Yu, J.; Low, J.; Fang, Y.; Xiao, J.; Chen, X. Engineering Heterogeneous Semiconductors for Solar Water Splitting. *J. Mater. Chem. A* **2015**, *3*, 2485−2534.
(37) Guijarro, N.; Prévot, M. S.; Sivula, K. Surface Modification of Semiconductor Photoelectrodes. *Phys. Chem. Chem. Phys.* **2015**, *17*, 15655−15674.
(38) Du, C.; Zhang, M.; Jang, J.-W.; Liu, Y.; Liu, G.-Y.; Wang, D. Observation and Alteration of Surface States of Hematite Photoelectrodes. *J. Phys. Chem. C* **2014**, *118*, 17054−17059.
(39) Fan, K.; Li, F.; Wang, L.; Daniel, Q.; Chen, H.; Gabrielsson, E.; Sun, J.; Sun, L. Immobilization of a Molecular Ruthenium Catalyst on Hematite Nanorod Arrays for Water Oxidation with Stable Photocurrent. *ChemSusChem* **2015**, *8*, 3242−3247.
(40) Jang, J.-W.; Du, C.; Ye, Y.; Lin, Y.; Yao, X.; Thorne, J.; Liu, E.; McMahon, G.; Zhu, J.; Javey, A.; et al. Enabling Unassisted Solar Water Splitting by Iron Oxide and Silicon. *Nat. Commun.* **2015**, *6*, 7447.
(41) Klahr, B.; Gimenez, S.; Fabregat-Santiago, F.; Bisquert, J.; Hamann, T. W. Photoelectrochemical and Impedance Spectroscopic Investigation of Water Oxidation with "Co-Pi"-Coated Hematite Electrodes. *J. Am. Chem. Soc.* **2012**, *134*, 16693−16700.
(42) Le Formal, F.; Sivula, K.; Grätzel, M. The Transient Photocurrent and Photovoltage Behavior of a Hematite Photoanode under Working Conditions and the Influence of Surface Treatments. *J. Phys. Chem. C* **2012**, *116*, 26707−26720.
(43) Le Formal, F.; Tétreault, N.; Cornuz, M.; Moehl, T.; Grätzel, M.; Sivula, K. Passivating Surface States on Water Splitting Hematite Photoanodes with Alumina Overlayers. *Chem. Sci.* **2011**, *2*, 737−743.
(44) Nellist, M. R.; Laskowski, F. A. L.; Lin, F.; Mills, T. J.; Boettcher, S. W. Semiconductor−Electrocatalyst Interfaces: Theory, Experiment, and Applications in Photoelectrochemical Water Splitting. *Acc. Chem. Res.* **2016**, *49*, 733−740.
(45) Smith, R. D. L.; Prevot, M. S.; Fagan, R. D.; Zhang, Z.; Sedach, P. A.; Siu, M. K. J.; Trudel, S.; Berlinguette, C. P. Photochemical Route for Accessing Amorphous Metal Oxide Materials for Water Oxidation Catalysis. *Science* **2013**, *340*, 60−63.
(46) Smith, R. D. L.; Prévot, M. S.; Fagan, R. D.; Trudel, S.; Berlinguette, C. P. Water Oxidation Catalysis: Electrocatalytic Response to Metal Stoichiometry in Amorphous Metal Oxide Films Containing Iron, Cobalt, and Nickel. *J. Am. Chem. Soc.* **2013**, *135*, 11580−11586.
(47) Smith, R. D. L.; Sporinova, B.; Fagan, R. D.; Trudel, S.; Berlinguette, C. P. Facile Photochemical Preparation of Amorphous Iridium Oxide Films for Water Oxidation Catalysis. *Chem. Mater.* **2014**, *26*, 1654−1659.
(48) Du, C.; Yang, X.; Mayer, M. T.; Hoyt, H.; Xie, J.; McMahon, G.; Bischoping, G.; Wang, D. Hematite-Based Water Splitting with Low Turn-On Voltages. *Angew. Chem., Int. Ed.* **2013**, *52*, 12692−12695.
(49) Indra, A.; Menezes, P. W.; Sahraie, N. R.; Bergmann, A.; Das, C.; Tallarida, M.; Schmeißer, D.; Strasser, P.; Driess, M. Unification of Catalytic Water Oxidation and Oxygen Reduction Reactions: Amorphous Beat Crystalline Cobalt Iron Oxides. *J. Am. Chem. Soc.* **2014**, *136*, 17530−17536.
(50) Tilley, S. D.; Cornuz, M.; Sivula, K.; Grätzel, M. Light-Induced Water Splitting with Hematite: Improved Nanostructure and Iridium Oxide Catalysis. *Angew. Chem., Int. Ed.* **2010**, *49*, 6405−6408.
(51) Yang, J.; Wang, D.; Han, H.; Li, C. Roles of Cocatalysts in Photocatalysis and Photoelectrocatalysis. *Acc. Chem. Res.* **2013**, *46*, 1900−1909.
(52) Ma, S. S. K.; Maeda, K.; Abe, R.; Domen, K. Visible-Light-Driven Nonsacrificial Water Oxidation over Tungsten Trioxide Powder Modified with Two Different Cocatalysts. *Energy Environ. Sci.* **2012**, *5*, 8390−8397.
(53) Bledowski, M.; Wang, L.; Neubert, S.; Mitoraj, D.; Beranek, R. Improving the Performance of Hybrid Photoanodes for Water Splitting by Photodeposition of Iridium Oxide Nanoparticles. *J. Phys. Chem. C* **2014**, *118*, 18951−18961.
(54) Strandwitz, N. C.; Comstock, D. J.; Grimm, R. L.; Nichols-Nielander, A. C.; Elam, J.; Lewis, N. S. Photoelectrochemical Behavior of N-type Si(100) Electrodes Coated with Thin Films of Manganese Oxide Grown by Atomic Layer Deposition. *J. Phys. Chem. C* **2013**, *117*, 4931−4936.

DOI: 10.1021/acs.jpcc.6b00735
J. Phys. Chem. C 2016, 120, 12999−13012

(55) Ye, H.; Park, H. S.; Bard, A. J. Screening of Electrocatalysts for Photoelectrochemical Water Oxidation on W-Doped $BiVO_4$ Photocatalysts by Scanning Electrochemical Microscopy. *J. Phys. Chem. C* **2011**, *115*, 12464−12470.
(56) Kim, T. W.; Choi, K.-S. Nanoporous $BiVO_4$ Photoanodes with Dual-Layer Oxygen Evolution Catalysts for Solar Water Splitting. *Science* **2014**, *343*, 990−994.
(57) Choi, S. K.; Choi, W.; Park, H. Solar Water Oxidation Using Nickel-Borate Coupled $BiVO_4$ Photoelectrodes. *Phys. Chem. Chem. Phys.* **2013**, *15*, 6499−6507.
(58) Jiang, C.; Moniz, S. J. A.; Khraisheh, M.; Tang, J. Earth-Abundant Oxygen Evolution Catalysts Coupled onto ZnO Nanowire Arrays for Efficient Photoelectrochemical Water Cleavage. *Chem. - Eur. J.* **2014**, *20*, 12954−12961.
(59) Yoshida, M.; Yomogida, T.; Mineo, T.; Nitta, K.; Kato, K.; Masuda, T.; Nitani, H.; Abe, H.; Takakusagi, S.; Uruga, T.; et al. Photoexcited Hole Transfer to a MnO_x Cocatalyst on a $SrTiO_3$ Photoelectrode during Oxygen Evolution Studied by In Situ X-ray Absorption Spectroscopy. *J. Phys. Chem. C* **2014**, *118*, 24302−24309.
(60) Zhong, D. K.; Gamelin, D. R. Photoelectrochemical Water Oxidation by Cobalt Catalyst ("Co-Pi")/α-Fe_2O_3 Composite Photoanodes: Oxygen Evolution and Resolution of a Kinetic Bottleneck. *J. Am. Chem. Soc.* **2010**, *132*, 4202−4207.
(61) Bediako, D. K.; Surendranath, Y.; Nocera, D. G. Mechanistic Studies of the Oxygen Evolution Reaction Mediated by a Nickel−Borate Thin Film Electrocatalyst. *J. Am. Chem. Soc.* **2013**, *135*, 3662−3674.
(62) Nocera, D. G. The Artificial Leaf. *Acc. Chem. Res.* **2012**, *45*, 767−776.
(63) de Respinis, M.; Joya, K. S.; De Groot, H. J. M.; D'Souza, F.; Smith, W. A.; van de Krol, R.; Dam, B. Solar Water Splitting Combining a $BiVO_4$ Light Absorber with a Ru-Based Molecular Cocatalyst. *J. Phys. Chem. C* **2015**, *119*, 7275−7281.
(64) Klepser, B. M.; Bartlett, B. M. Anchoring a Molecular Iron Catalyst to Solar-Responsive WO_3 Improves the Rate and Selectivity of Photoelectrochemical Water Oxidation. *J. Am. Chem. Soc.* **2014**, *136*, 1694−1697.
(65) Chen, X. J.; Ren, X. D.; Liu, Z. L.; Zhuang, L.; Lu, J. T. Promoting the Photoanode Efficiency for Water Splitting by Combining Hematite and Molecular Ru Catalysts. *Electrochem. Commun.* **2013**, *27*, 148−151.
(66) Karkas, M. D.; Verho, O.; Johnston, E. V.; Åkermark, B. Artificial Photosynthesis: Molecular Systems for Catalytic Water Oxidation. *Chem. Rev.* **2014**, *114*, 11863−12001.
(67) Francàs, L.; Bofill, R.; García-Antón, J.; Escriche, L.; Sala, X.; Llobet, A. Ru-Based Water Oxidation Catalysts. In *Molecular Water Oxidation Catalysts*; Llobet, A., Ed.; John Wiley and Sons, Inc.: Chichester, West Sussex, U.K., 2014; pp 29−50.
(68) Blakemore, J. D.; Crabtree, R. H.; Brudvig, G. W. Molecular Catalysts for Water Oxidation. *Chem. Rev.* **2015**, *115*, 12974−13005.
(69) Limburg, B.; Bouwman, E.; Bonnet, S. Molecular Water Oxidation Catalysts Based on Transition Metals and Their Decomposition Pathways. *Coord. Chem. Rev.* **2012**, *256*, 1451−1467.
(70) Artero, V.; Fontecave, M. Solar Fuels Generation and Molecular Systems: Is It Homogeneous or Heterogeneous Catalysis? *Chem. Soc. Rev.* **2013**, *42*, 2338−2356.
(71) Harriman, A. Photo-Oxidation of Water under Ambient Conditions - The Search for Effective Oxygen-Evolving Catalysts. *Eur. J. Inorg. Chem.* **2014**, *2014*, 573−580.
(72) Hintermair, U.; Hashmi, S. M.; Elimelech, M.; Crabtree, R. H. Particle Formation during Oxidation Catalysis with Cp* Iridium Complexes. *J. Am. Chem. Soc.* **2012**, *134*, 9785−9795.
(73) Thomsen, J. M.; Huang, D. L.; Crabtree, R. H.; Brudvig, G. W. Iridium-Based Complexes for Water Oxidation. *Dalt. Trans.* **2015**, *44*, 12452−12472.
(74) Hintermair, U.; Sheehan, S. W.; Parent, A. R.; Ess, D. H.; Richens, D. T.; Vaccaro, P. H.; Brudvig, G. W.; Crabtree, R. H. Precursor Transformation during Molecular Oxidation Catalysis with Organometallic Iridium Complexes. *J. Am. Chem. Soc.* **2013**, *135*, 10837−10851.
(75) Ingram, A. J.; Wolk, A. B.; Flender, C.; Zhang, J.; Johnson, C. J.; Hintermair, U.; Crabtree, R. H.; Johnson, M. A.; Zare, R. N. Modes of Activation of Organometallic Iridium Complexes for Catalytic Water and C−H Oxidation. *Inorg. Chem.* **2014**, *53*, 423−433.
(76) Thomsen, J. M.; Sheehan, S. W.; Hashmi, S. M.; Campos, J.; Hintermair, U.; Crabtree, R. H.; Brudvig, G. W. Electrochemical Activation of Cp* Iridium Complexes for Electrode-Driven Water-Oxidation Catalysis. *J. Am. Chem. Soc.* **2014**, *136*, 13826−13834.
(77) Sheehan, S. W.; Thomsen, J. M.; Hintermair, U.; Crabtree, R. H.; Brudvig, G. W.; Schmuttenmaer, C. A. A Molecular Catalyst for Water Oxidation That Binds to Metal Oxide Surfaces. *Nat. Commun.* **2015**, *6*, 6469.
(78) Li, W.; Sheehan, S. W.; He, D.; He, Y.; Yao, X.; Grimm, R. L.; Brudvig, G. W.; Wang, D. Hematite-Based Solar Water Splitting in Acidic Solutions: Functionalization by Mono- and Multilayers of Iridium Oxygen-Evolution Catalysts. *Angew. Chem., Int. Ed.* **2015**, *54*, 11428−11432.
(79) Moir, J.; Soheilnia, N.; O'Brien, P.; Jelle, A.; Grozea, C. M.; Faulkner, D.; Helander, M. G.; Ozin, G. A. Enhanced Hematite Water Electrolysis Using a 3D Antimony-Doped Tin Oxide Electrode. *ACS Nano* **2013**, *7*, 4261−4274.
(80) Redel, E.; Mirtchev, P.; Huai, C.; Petrov, S.; Ozin, G. A. Nanoparticle Films and Photonic Crystal Multilayers from Colloidally Stable, Size-Controllable Zinc and Iron Oxide Nanoparticles. *ACS Nano* **2011**, *5*, 2861−2869.
(81) Boudoire, F.; Toth, R.; Heier, J.; Braun, A.; Constable, E. C. Photonic Light Trapping in Self-Organized All-Oxide Microspheroids Impacts Photoelectrochemical Water Splitting. *Energy Environ. Sci.* **2014**, *7*, 2680−2688.
(82) Klahr, B.; Hamann, T. Water Oxidation on Hematite Photoelectrodes: Insight into the Nature of Surface States through In Situ Spectroelectrochemistry. *J. Phys. Chem. C* **2014**, *118*, 10393−10399.
(83) Kay, A.; Cesar, I.; Grätzel, M. New Benchmark for Water Photooxidation by Nanostructured α-Fe_2O_3 Films. *J. Am. Chem. Soc.* **2006**, *128*, 15714−15721.
(84) Klahr, B.; Gimenez, S.; Fabregat-Santiago, F.; Hamann, T.; Bisquert, J. Water Oxidation at Hematite Photoelectrodes: The Role of Surface States. *J. Am. Chem. Soc.* **2012**, *134*, 4294−4302.
(85) Glasscock, J. A.; Barnes, P. R. F.; Plumb, I. C.; Bendavid, A.; Martin, P. J. Structural, Optical and Electrical Properties of Undoped Polycrystalline Hematite Thin Films Produced Using Filtered Arc Deposition. *Thin Solid Films* **2008**, *516*, 1716−1724.
(86) Zhao, Y.; Vargas-Barbosa, N. M.; Strayer, M. E.; McCool, N. S.; Pandelia, M.-E.; Saunders, T. P.; Swierk, J. R.; Callejas, J. F.; Jensen, L.; Mallouk, T. E. Understanding the Effect of Monomeric Iridium(III/IV) Aquo Complexes on the Photoelectrochemistry of $IrO_x{\cdot}nH_2O$-Catalyzed Water-Splitting Systems. *J. Am. Chem. Soc.* **2015**, *137*, 8749−8757.
(87) Wang, G.; Wang, H.; Ling, Y.; Tang, Y.; Yang, X.; Fitzmorris, R. C.; Wang, C.; Zhang, J. Z.; Li, Y. Hydrogen-Treated TiO2 Nanowire Arrays for Photoelectrochemical Water Splitting. *Nano Lett.* **2011**, *11* (7), 3026−3033.
(88) Klahr, B.; Gimenez, S.; Fabregat-Santiago, F.; Bisquert, J.; Hamann, T. W. Electrochemical and Photoelectrochemical Investigation of Water Oxidation with Hematite Electrodes. *Energy Environ. Sci.* **2012**, *5*, 7626−7636.
(89) Bertoluzzi, L.; Bisquert, J. Equivalent Circuit of Electrons and Holes in Thin Semiconductor Films for Photoelectrochemical Water Splitting Applications. *J. Phys. Chem. Lett.* **2012**, *3*, 2517−2522.
(90) Bisquert, J.; Garcia-Belmonte, G.; Fabregat-Santiago, F.; Compte, A. Anomalous Transport Effects in the Impedance of Porous Film Electrodes. *Electrochem. Commun.* **1999**, *1*, 429−435.
(91) Bisquert, J. Influence of the Boundaries in the Impedance of Porous Film Electrodes. *Phys. Chem. Chem. Phys.* **2000**, *2*, 4185−4192.
(92) Badia-Bou, L.; Mas-Marza, E.; Rodenas, P.; Barea, E. M.; Fabregat-Santiago, F.; Gimenez, S.; Peris, E.; Bisquert, J. Water

DOI: 10.1021/acs.jpcc.6b00735
J. Phys. Chem. C 2016, 120, 12999−13012

Oxidation at Hematite Photoelectrodes with an Iridium-Based Catalyst. *J. Phys. Chem. C* **2013**, *117*, 3826−3833.
(93) Li, W.; He, D.; Sheehan, S. W.; He, Y.; Thorne, J. E.; Yao, X.; Brudvig, G.; Wang, D. Comparison of Heterogenized Molecular and Heterogeneous Oxide Catalysts for Photoelectrochemical Water Oxidation. *Energy Environ. Sci.* **2016**, *9*, 1794−1802.
(94) Peter, L. M. Energetics and Kinetics of Light-Driven Oxygen Evolution at Semiconductor Electrodes: The Example of Hematite. *J. Solid State Electrochem.* **2013**, *17*, 315−326.
(95) Peter, L. M.; Wijayantha, K. G. U.; Tahir, A. A. Kinetics of Light-Driven Oxygen Evolution at α-Fe_2O_3 Electrodes. *Faraday Discuss.* **2012**, *155*, 309−322.
(96) Peter, L. M.; Upul Wijayantha, K. G. Photoelectrochemical Water Splitting at Semiconductor Electrodes: Fundamental Problems and New Perspectives. *ChemPhysChem* **2014**, *15*, 1983−1995.
(97) Peter, L. M. Dynamic Aspects of Semiconductor Photoelectrochemistry. *Chem. Rev.* **1990**, *90*, 753−769.
(98) Dotan, H.; Sivula, K.; Grätzel, M.; Rothschild, A.; Warren, S. C. Probing the Photoelectrochemical Properties of Hematite (α-Fe_2O_3) Electrodes Using Hydrogen Peroxide as a Hole Scavenger. *Energy Environ. Sci.* **2011**, *4*, 958−964.
(99) Le Formal, F.; Pastor, E.; Tilley, S. D.; Mesa, C. A.; Pendlebury, S. R.; Grätzel, M.; Durrant, J. R. Rate Law Analysis of Water Oxidation on a Hematite Surface. *J. Am. Chem. Soc.* **2015**, *137*, 6629−6637.
(100) Upul Wijayantha, K. G.; Saremi-Yarahmadi, S.; Peter, L. M. Kinetics of Oxygen Evolution at α-Fe_2O_3 Photoanodes: A Study by Photoelectrochemical Impedance Spectroscopy. *Phys. Chem. Chem. Phys.* **2011**, *13*, 5264−5270.
(101) Duret, A.; Grätzel, M. Visible Light-Induced Water Oxidation on Mesoscopic α-Fe_2O_3 Films Made by Ultrasonic Spray Pyrolysis. *J. Phys. Chem. B* **2005**, *109*, 17184−17191.

DOI: 10.1021/acs.jpcc.6b00735
J. Phys. Chem. C 2016, 120, 12999−13012